Supporting Information

Doping and Pretreatment Optimized the Adsorption of *OCHO on Bismuth for Electrocatalytic Reduction CO_2 to Formate

Meng Tian,[a] Shanshan Wu,[a] Yang Hu,[a] Zhaori Mu,[a] Zhi Li,[a] Yichao Hou,[a] Pinxian Xi*[a] and Chun-Hua Yan[a,b]

[a] State Key Laboratory of Applied Organic Chemistry, Frontiers Science Center for Rare Isotopes, College of Chemistry and Chemical Engineering, Lanzhou University, Lanzhou 730000, China, E-mail: xipx@lzu.edu.cn

[b] Beijing National Laboratory for Molecular Sciences, State Key Laboratory of Rare Earth Materials Chemistry and Applications, PKU-HKU Joint Laboratory in Rare Earth Materials and Bioinorganic Chemistry, College of Chemistry and Molecular Engineering Peking University, Beijing 100871, China

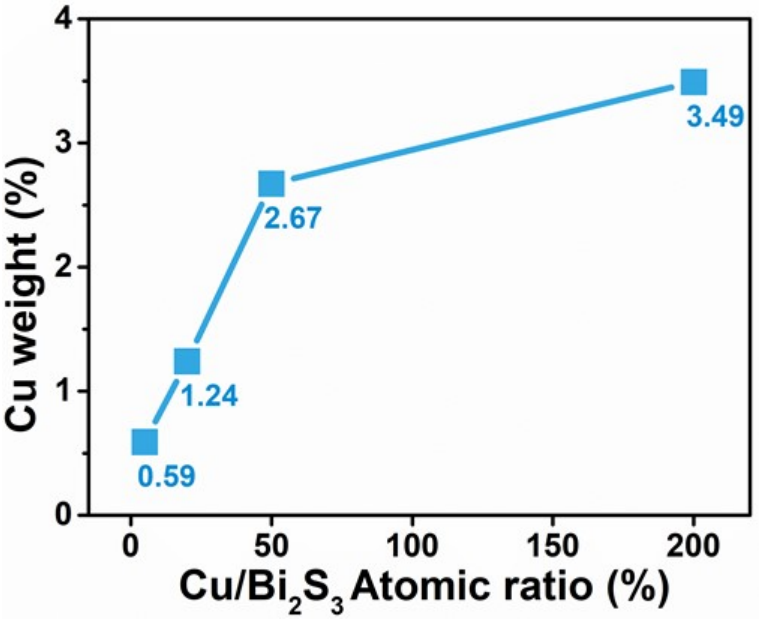

Fig. S1 ICP images of Cu-doped Bi_2S_3 samples.

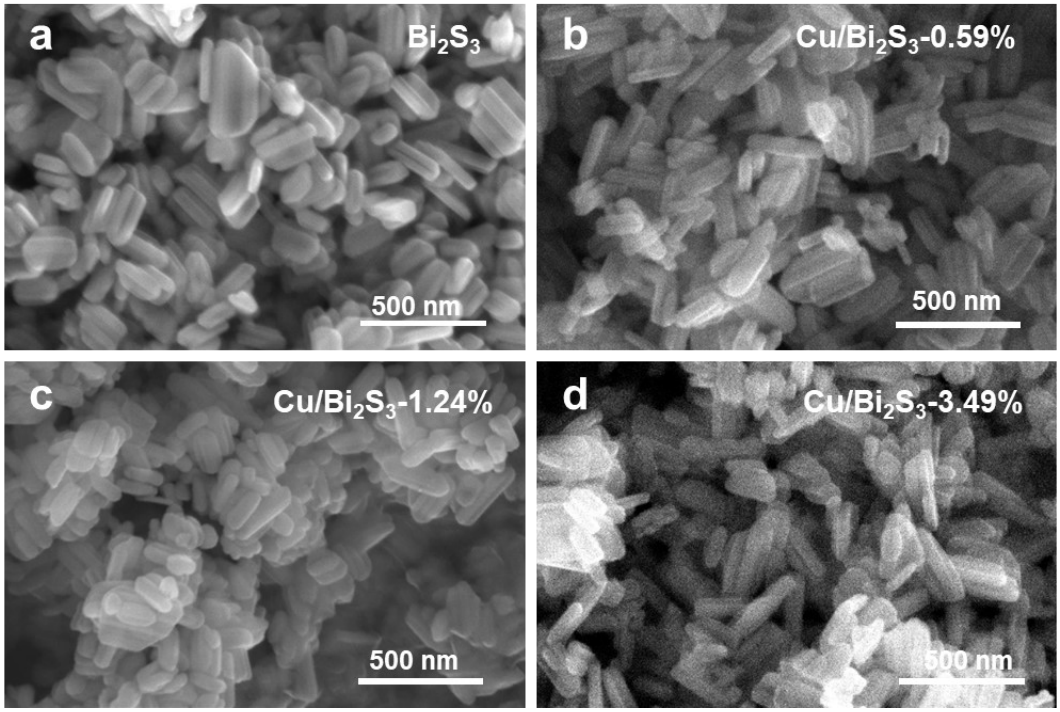

Fig. S2 SEM images of Bi_2S_3 (a), Cu/Bi_2S_3-0.59% (b), Cu/Bi_2S_3-1.24% (c) and Cu/Bi_2S_3-3.49% (d).

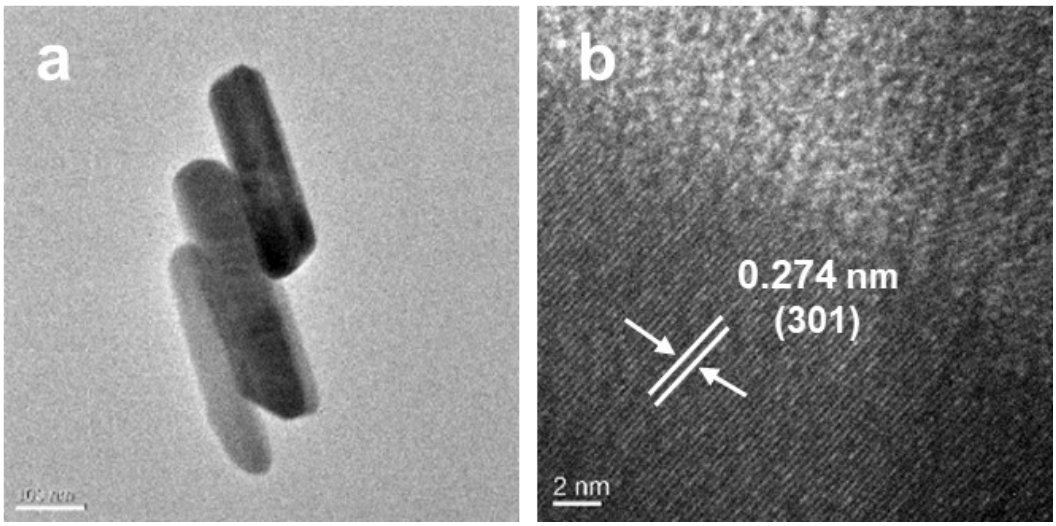

Fig. S3 TEM (a) and HRTEM (b) images of Bi_2S_3.

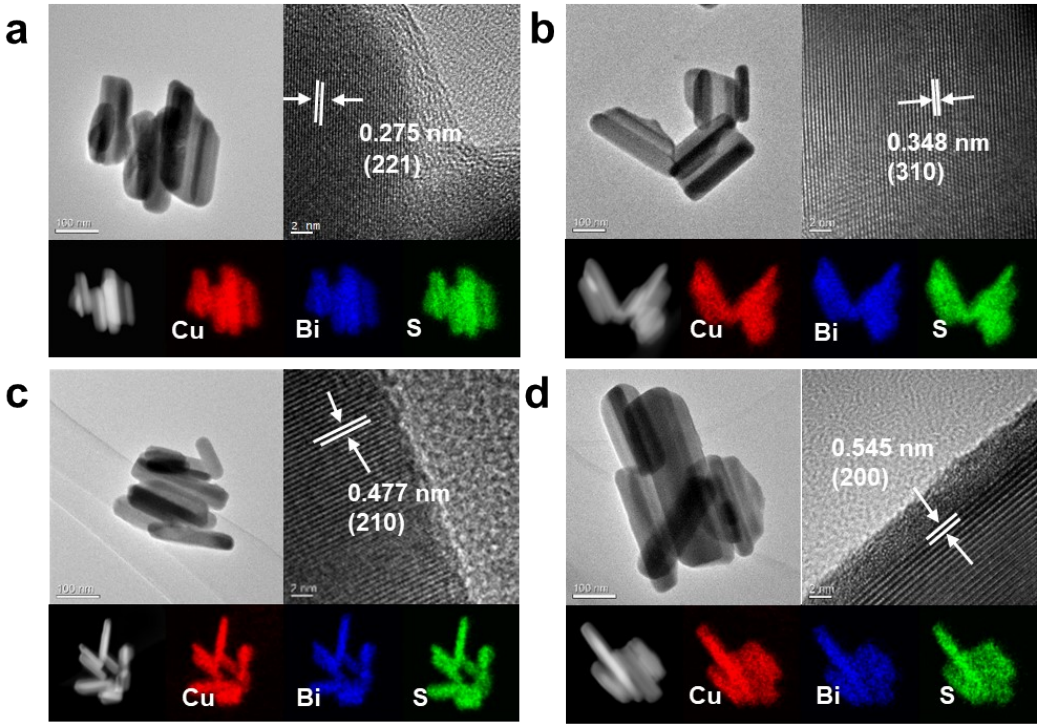

Fig. S4 TEM, HRTEM and corresponding elemental mapping images of Cu/Bi_2S_3-0.59% (a), Cu/Bi_2S_3-1.24% (b), Cu/Bi_2S_3-2.67% (c) and Cu/Bi_2S_3-3.49% (d).

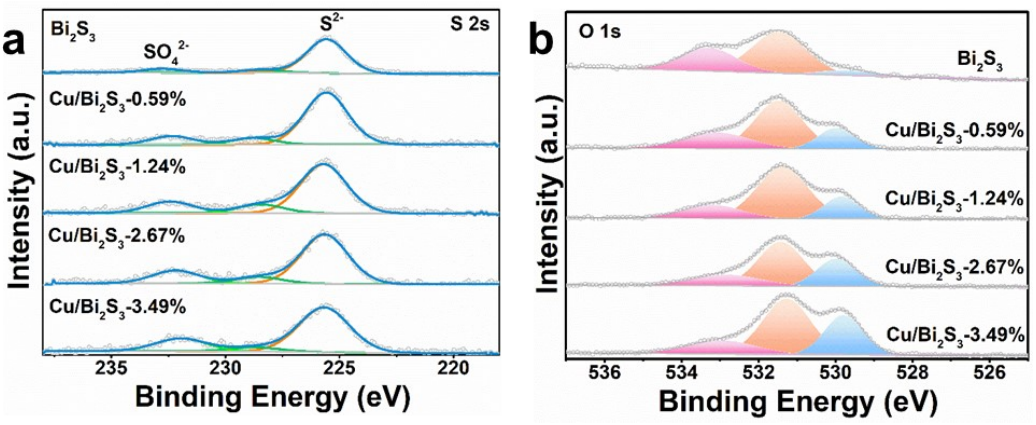

Fig. S5 (a) S 2s XPS spectra and (b) O 1s XPS spectra of Bi_2S_3, Cu/Bi_2S_3-0.59%, Cu/Bi_2S_3-1.24%, Cu/Bi_2S_3-2.67% and Cu/Bi_2S_3-3.49%.

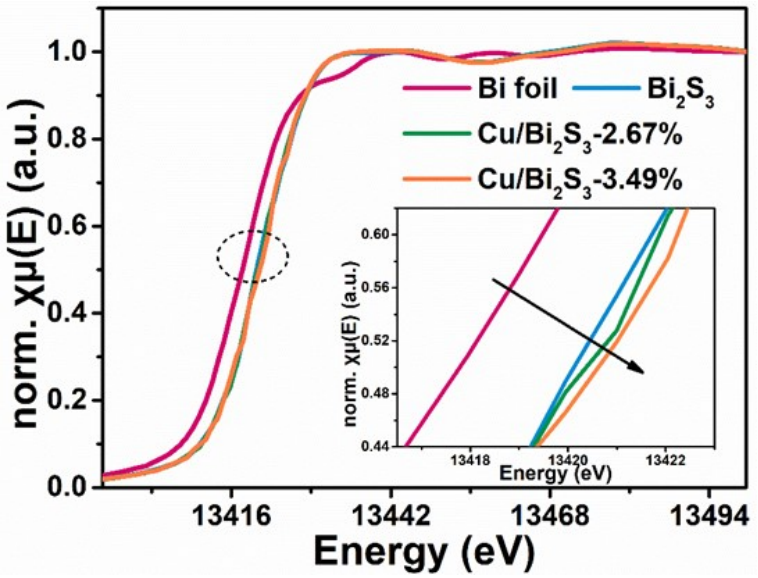

Fig. S6 Bi L_3-edge XANES spectra (the inset is a partial enlargement).

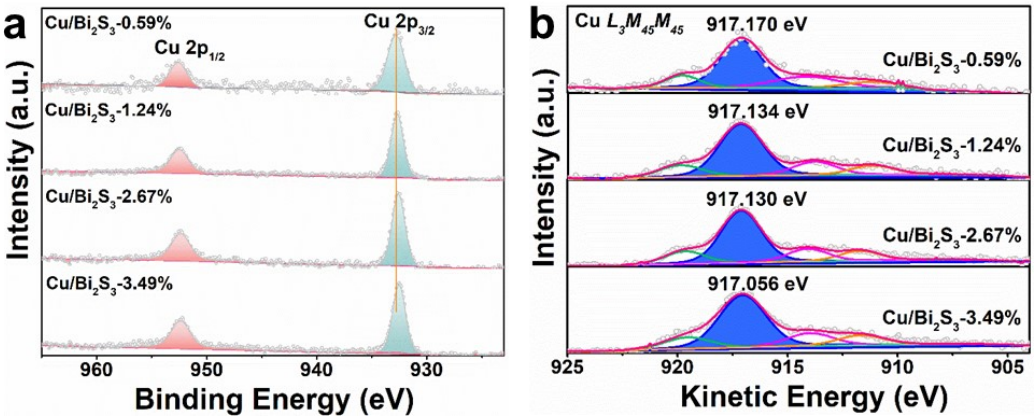

Fig. S7 (a) Cu 2p XPS spectra and (b) Cu $L_3M_{45}M_{45}$ Auger spectroscopy of Cu/Bi_2S_3-0.59%, Cu/Bi_2S_3-1.24%, Cu/Bi_2S_3-2.67% and Cu/Bi_2S_3-3.49%.

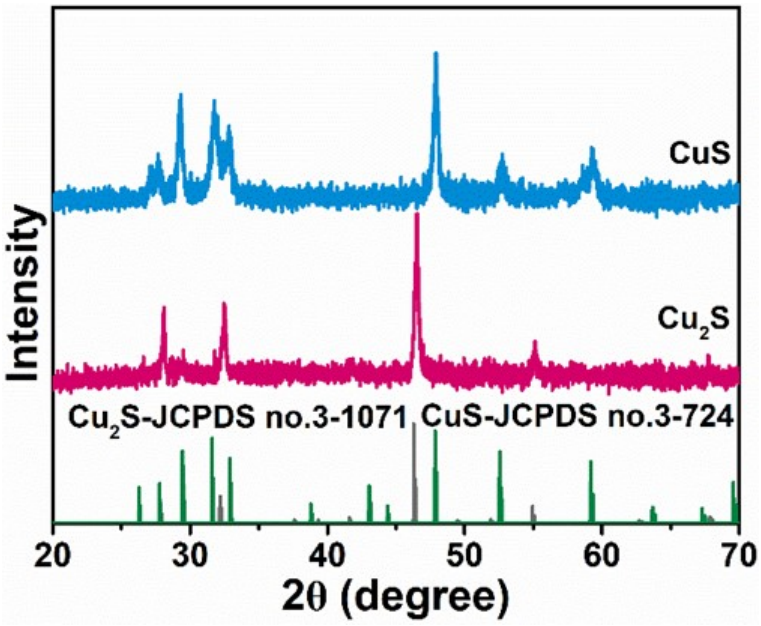

Fig. S8 XRD patterns of Cu_2S and CuS.

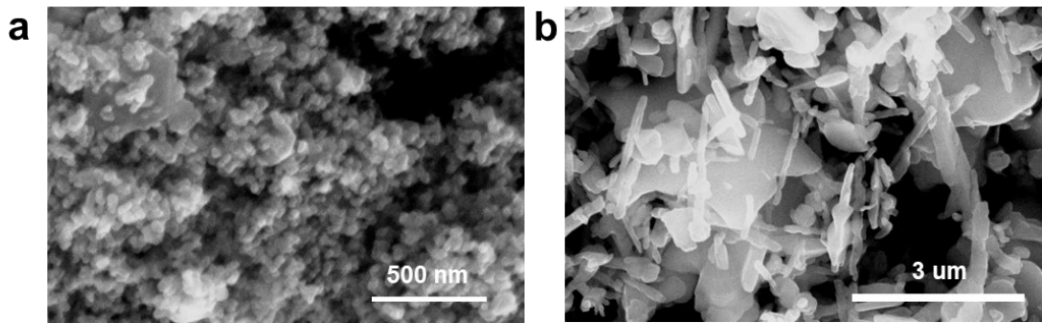

Fig. S9 SEM images of CuS (a) and Cu_2S (b).

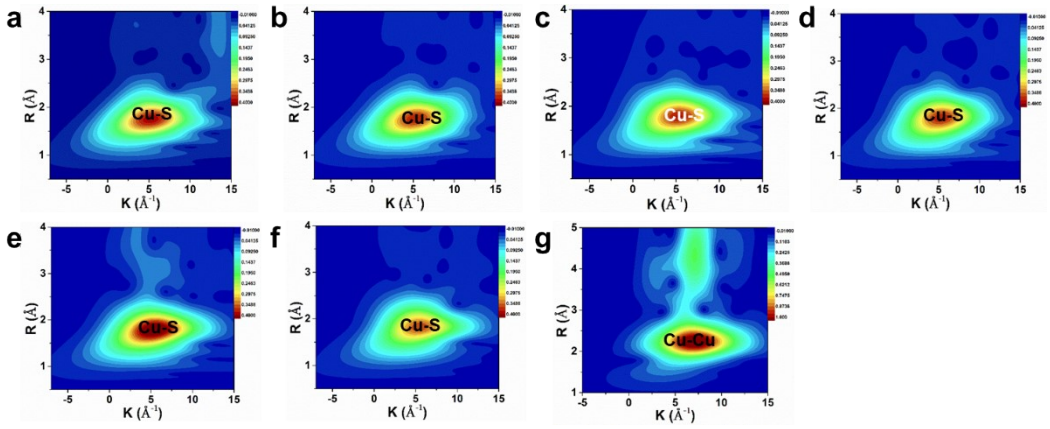

Fig. S10 The corresponding wavelet transforms for Cu K-edge EXAFS signals of Cu/Bi_2S_3-0.59% (a), Cu/Bi_2S_3-1.24% (b), Cu/Bi_2S_3-2.67% (c) Cu/Bi_2S_3-3.49% (d), CuS (e), Cu_2S (f), and Cu foil (g).

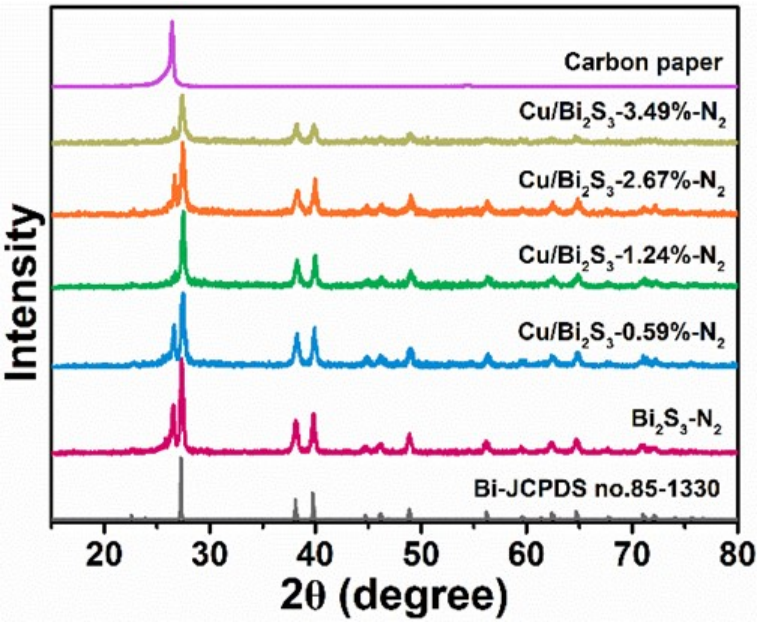

Fig. S11 XRD patterns of the different samples.

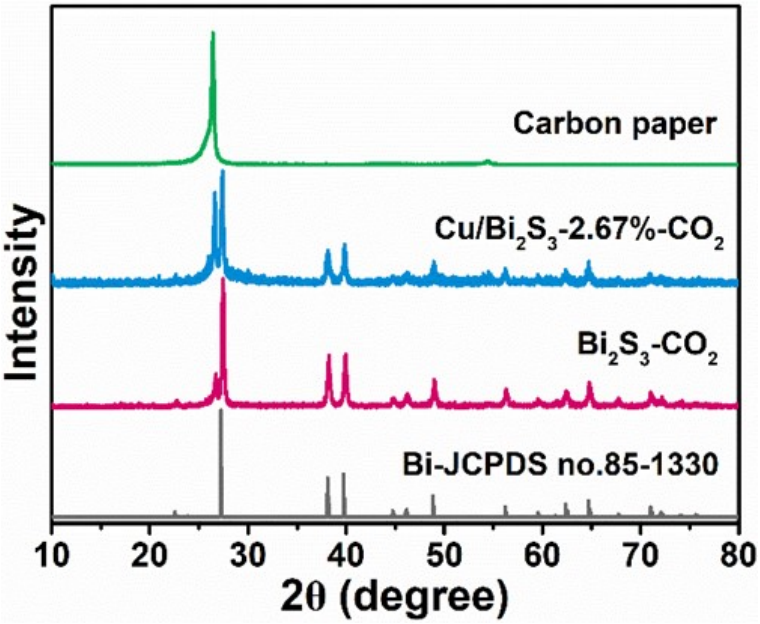

Fig. S12 XRD patterns of Bi_2S_3-CO_2, Cu/Bi_2S_3-2.67%-CO_2 and carbon paper.

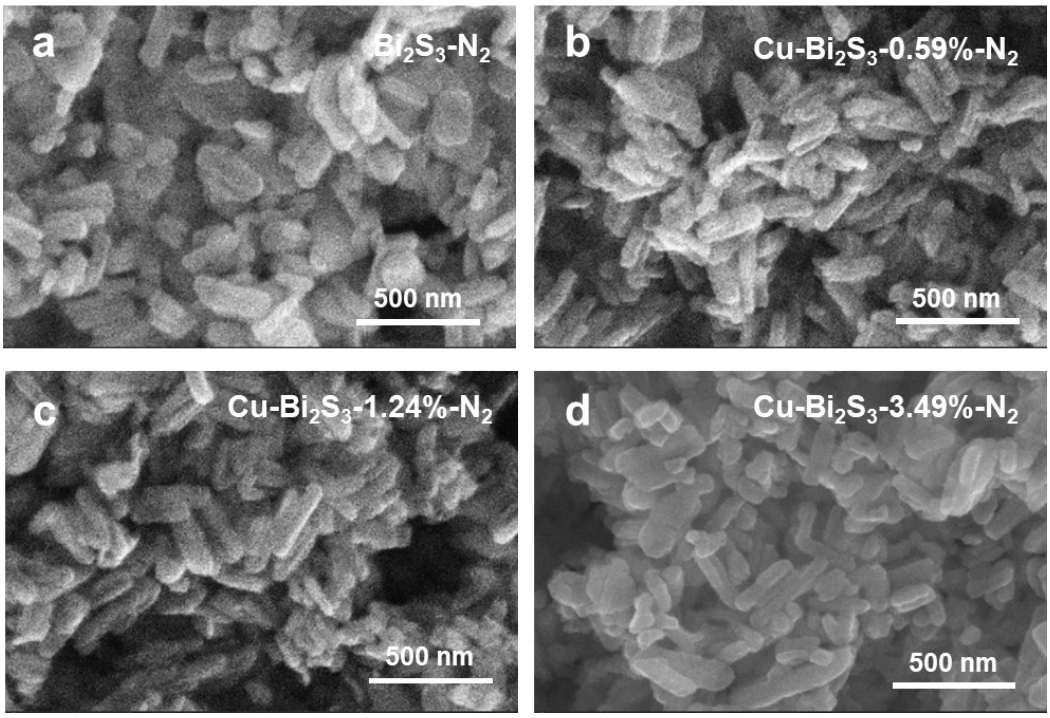

Fig. S13 SEM images of Bi_2S_3-N_2 (a), Cu/Bi_2S_3-0.59%-N_2 (b), Cu/Bi_2S_3-1.24%-N_2 (c) and Cu/Bi_2S_3-3.49%-N_2 (d).

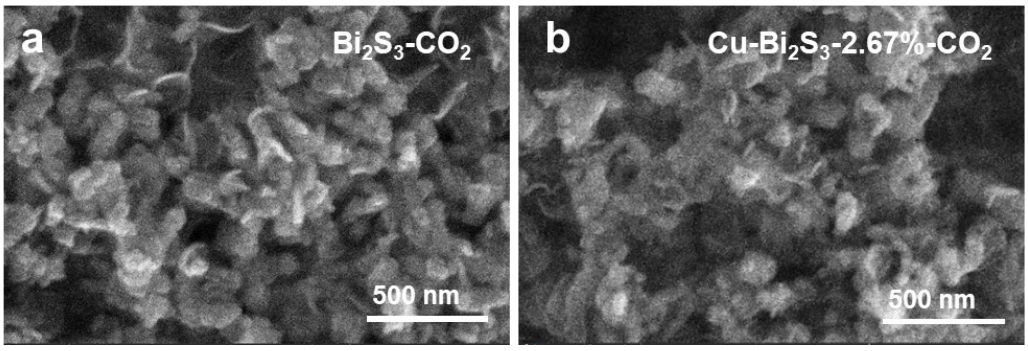

Fig. S14 SEM images of Bi_2S_3-CO_2 (a), Cu/Bi_2S_3-2.67%-CO_2 (b).

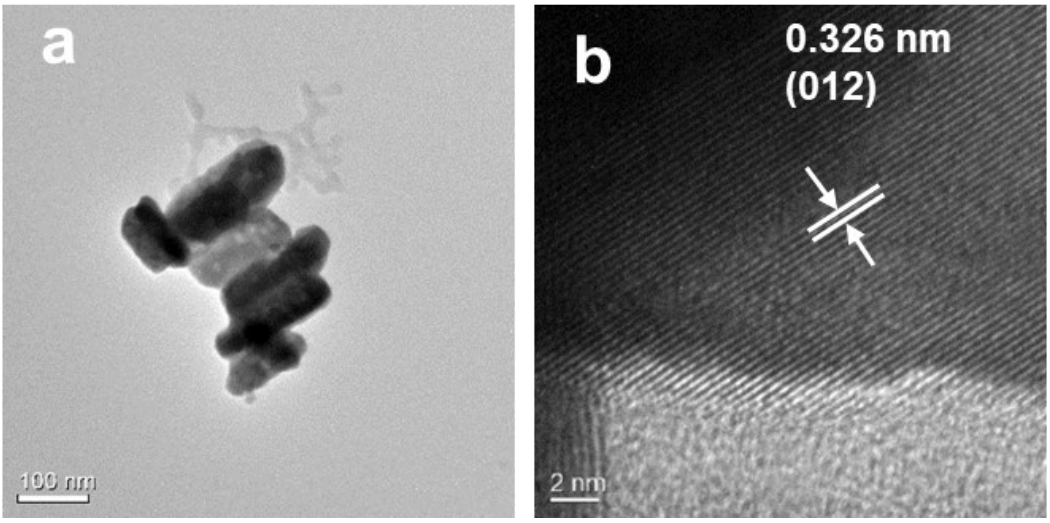

Fig. S15 TEM (a) and HRTEM (b) images of Bi_2S_3-N_2.

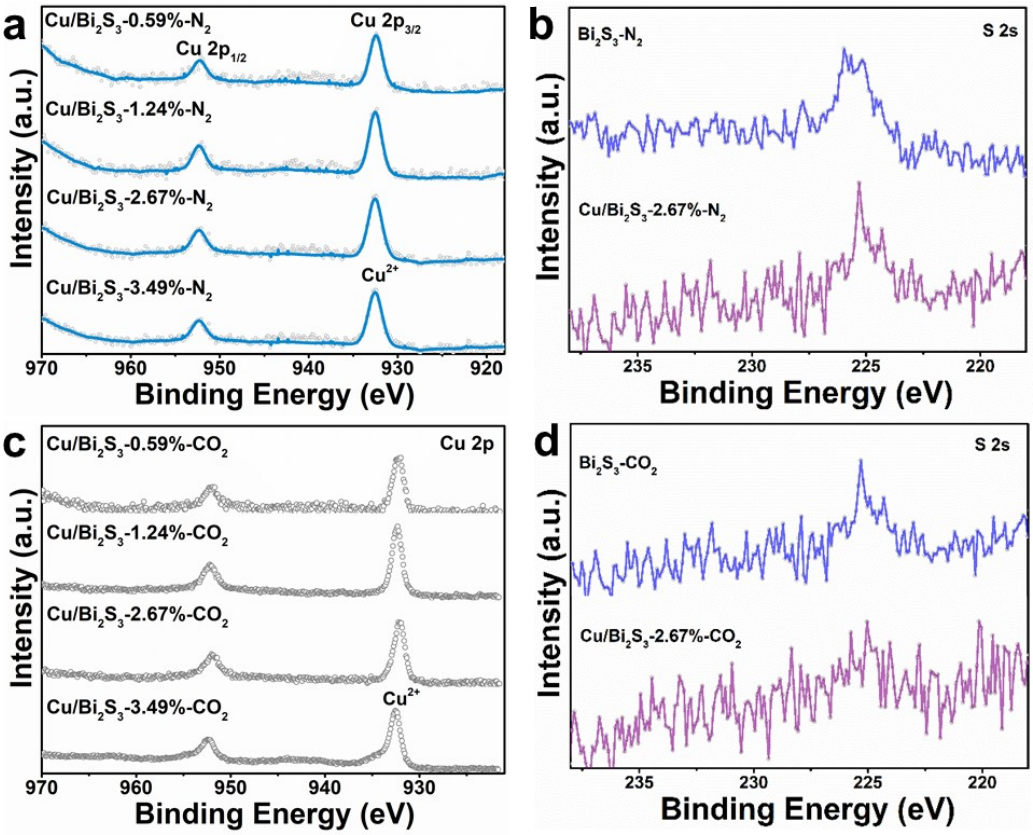

Fig. S16 (a) Cu 2p XPS spectra and (b) S 2s XPS spectra of the different samples. (c) Cu 2p XPS spectra and (d) S 2s XPS spectra of the different samples.

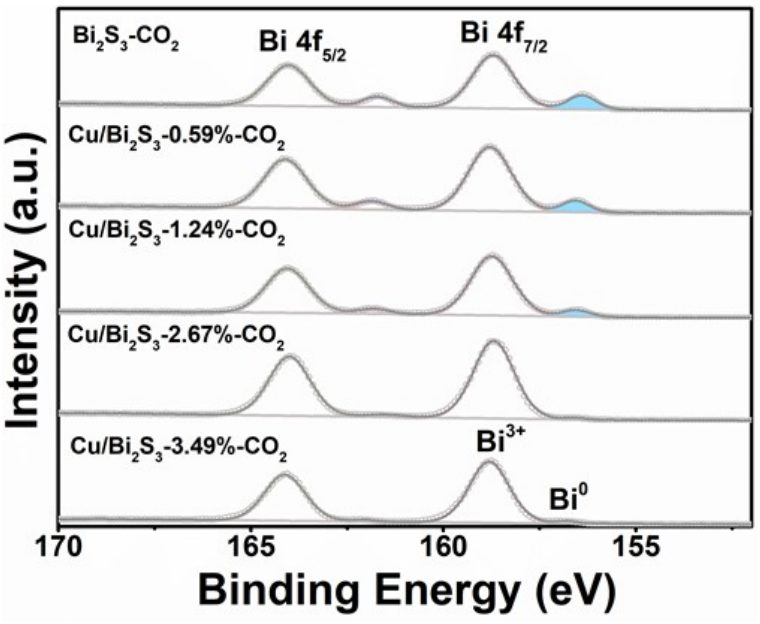

Fig. S17 Bi 4f XPS spectra Cu/Bi_2S_3-x-CO_2 catalysts (x = 0.59%, 1.24%, 2.67%, 3.49%).

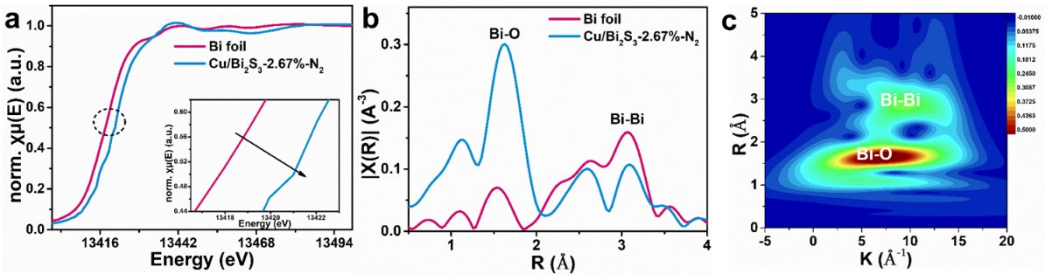

Fig. S18 (a) Bi L_3-edge XANES spectra (the inset is a partial enlargement), (b) Bi L_3-edge FT-EXAFS spectra in R space. (c) The corresponding wavelet transforms of Bi L_3-edge EXAFS signal of Cu/Bi_2S_3-2.67%-N_2.

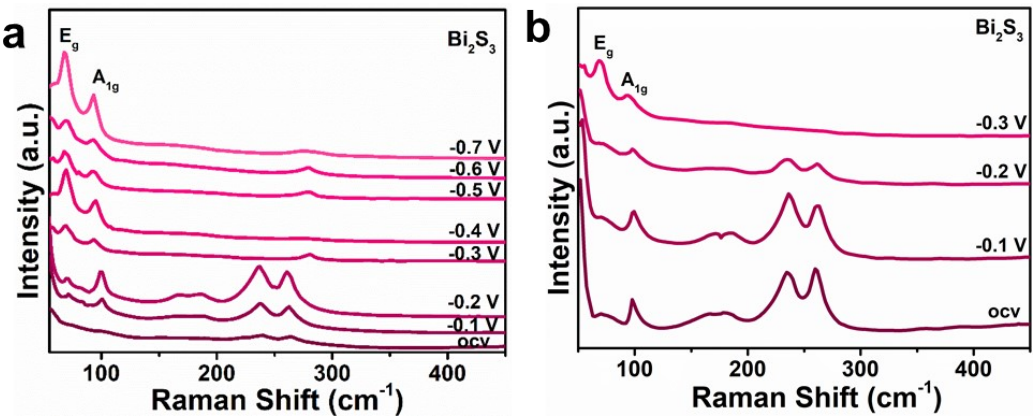

Fig. S19 Potential-dependent in situ Raman spectra of Bi_2S_3 in N_2-saturated $KHCO_3$ solution (a) and CO_2-saturated $KHCO_3$ solution (b).

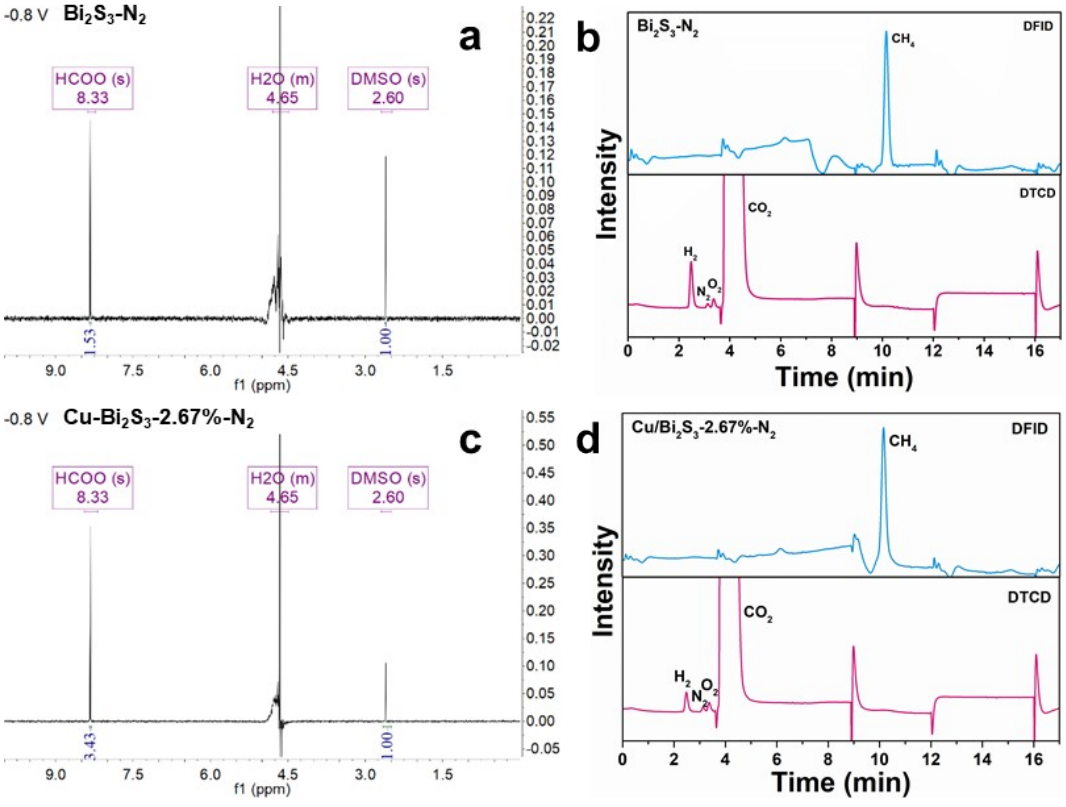

Fig. S20 Nuclear magnetic mass spectrometry (a, c) and gas chromatography (b, d) of Bi_2S_3-N_2 and Cu/Bi_2S_3-2.67%-N_2 at -0.8 V vs. RHE, respectively.

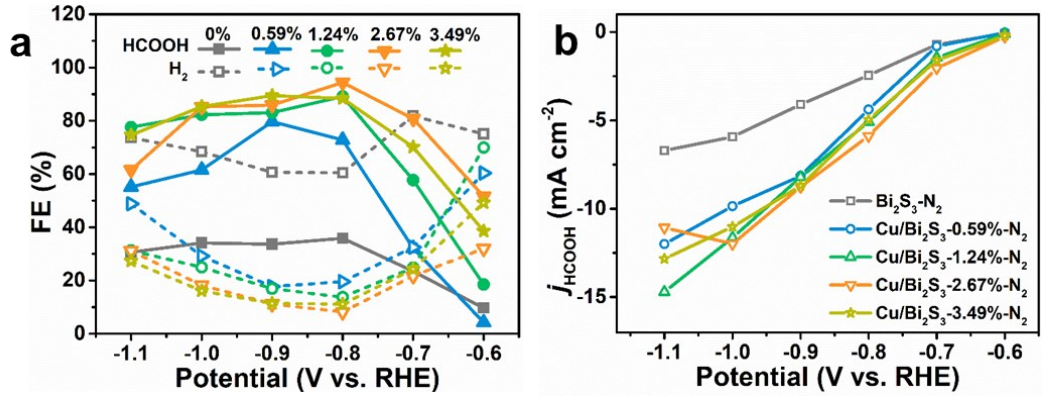

Fig. S21 (a) Potential-dependent Faradaic efficiencies of H_2 and HCOOH for Bi_2S_3-N_2, Cu/Bi_2S_3-0.59%-N_2, Cu/Bi_2S_3-1.24%-N_2, Cu/Bi_2S_3-2.67%-N_2 and Cu/Bi_2S_3-3.49%-N_2 in CO_2-saturated 0.5 M $KHCO_3$. (b) Potential-dependent HCOOH partial current densities of the different samples.

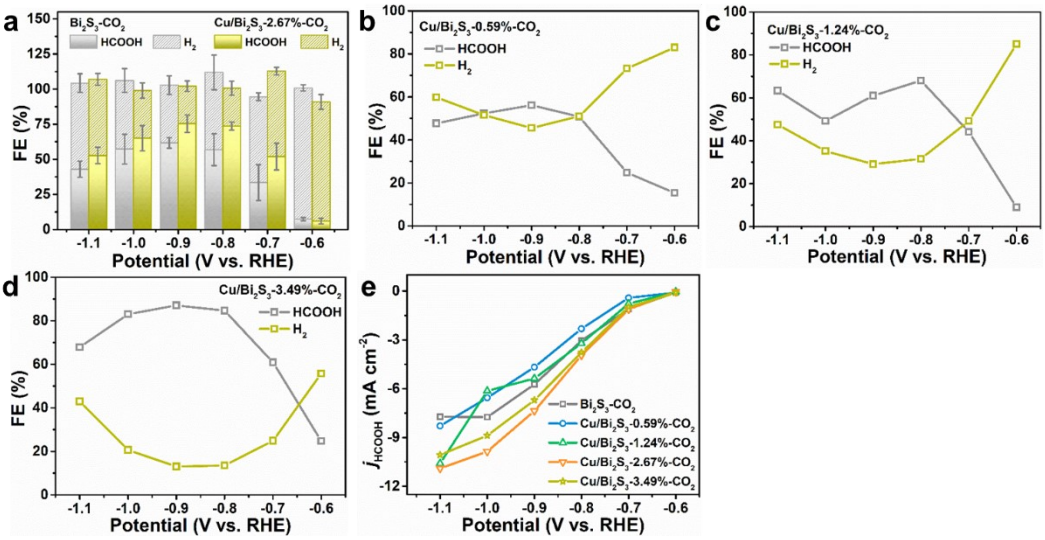

Fig. S22 (a) Potential-dependent Faradaic efficiencies of H_2 and HCOOH for Bi_2S_3-CO_2 and Cu/Bi_2S_3-2.67%-CO_2 in CO_2-saturated 0.5 M $KHCO_3$. Potential-dependent Faradaic efficiencies of H_2 and HCOOH for Cu/Bi_2S_3-0.59%-CO_2 (b), Cu/Bi_2S_3-1.24%-CO_2 (c), and Cu/Bi_2S_3-3.49%-CO_2 (d). (e) Potential-dependent HCOOH partial current densities of the different samples.

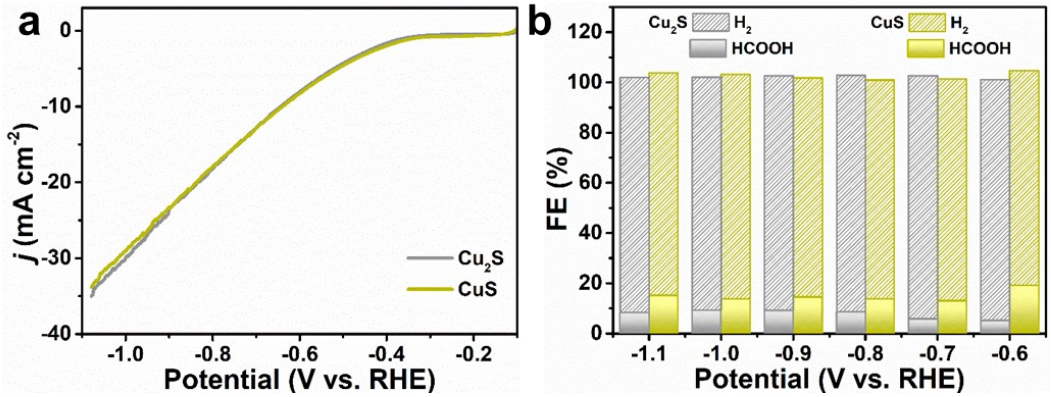

Fig. S23 (a)LSV curves of Cu_2S and CuS under CO_2-saturated 0.5 M $KHCO_3$ electrolyte. (b) FEs of H_2 and HCOOH for Cu_2S and CuS at different potentials.

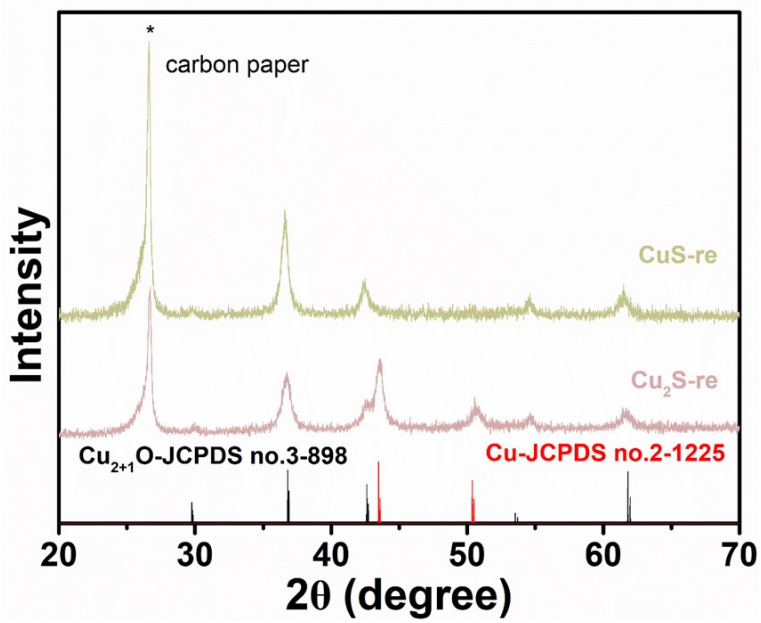

Fig. S24 XRD patterns of Cu_2S and CuS after ECO_2R.

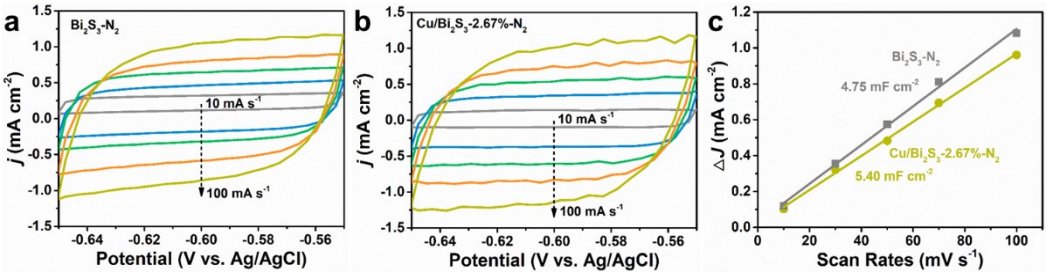

Fig. S25 CV curves in the region of -0.65 ~ -0.55 V vs. Ag/AgCl at various scan rate (10 ~ 100 mV s^{-1}) of Bi_2S_3-N_2 (a), Cu/Bi_2S_3-2.67%-N_2 (b). (c) C_{dl} of those materials.

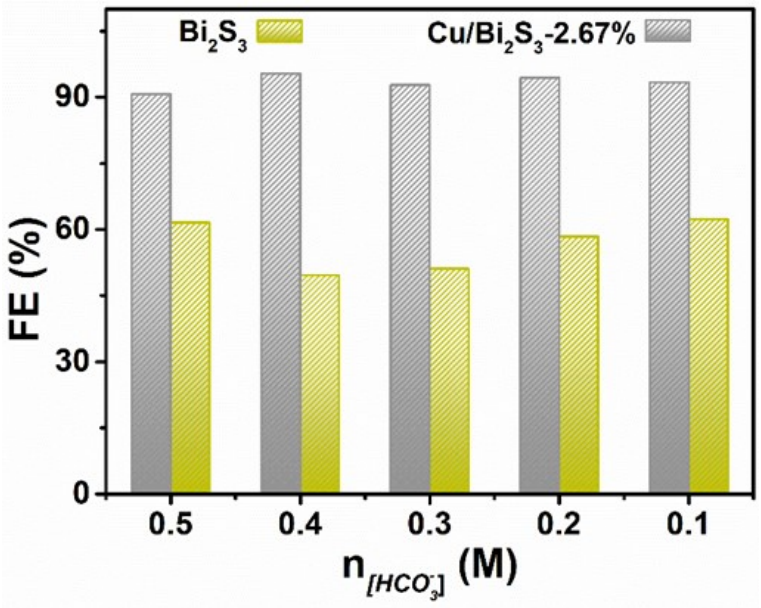

Fig. S26 FEs of HCOOH for Bi_2S_3-N_2 and Cu/Bi_2S_3-2.67%-N_2 at the different concentration of bicarbonate.

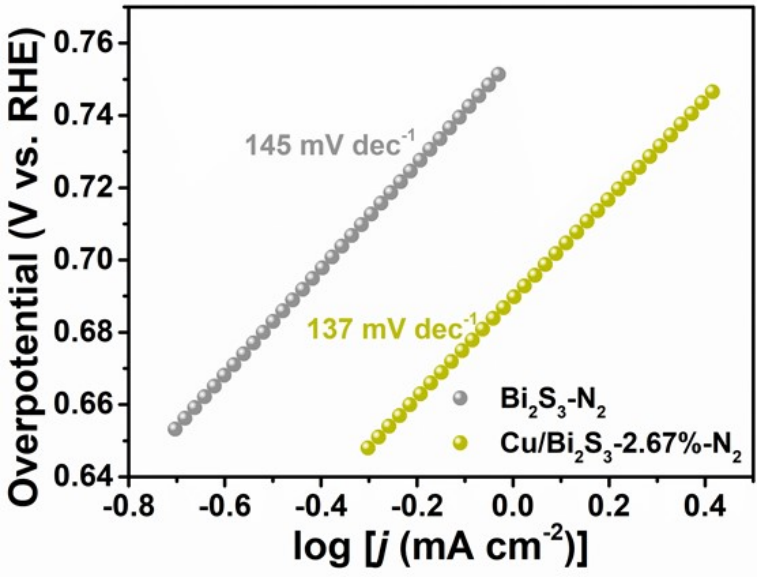

Fig. S27 Tafel plots of different catalysts for HCOOH production.

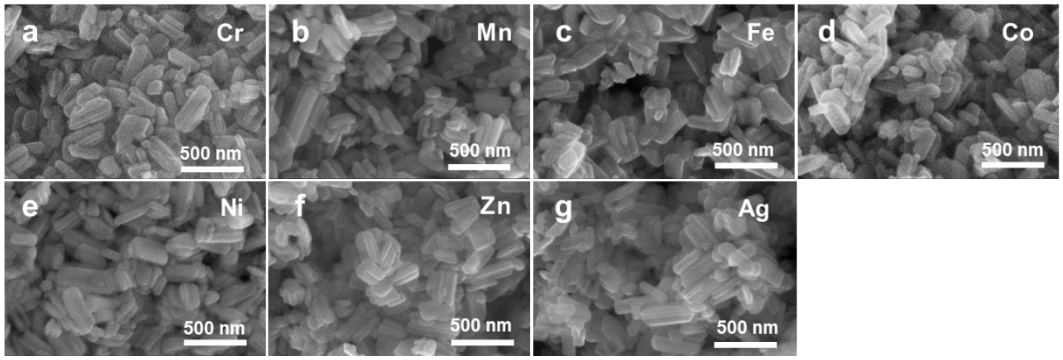

Fig. S28 SEM images of Bi_2S_3 after introducing different metal elements (Cr, Mn, Fe, Co, Ni, Zn, Ag) respectively.

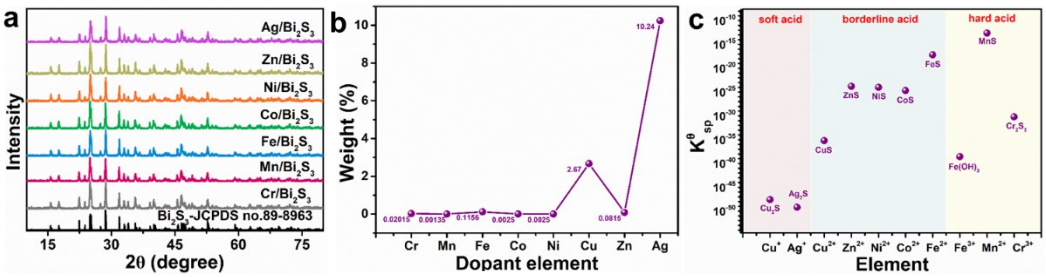

Fig. S29 (a) XRD patterns and (b) ICP images of Bi_2S_3 doped with different metal elements. (c) Ksp images of different compounds.

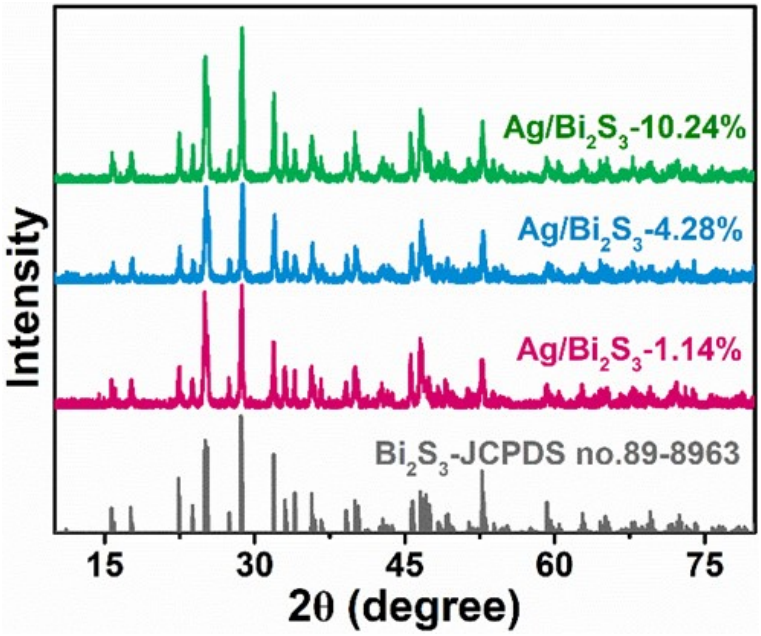

Fig. S30 XRD patterns of Ag/Bi_2S_3-1.14%, Ag/Bi_2S_3-4.28%, and Ag/Bi_2S_3-10.24%.

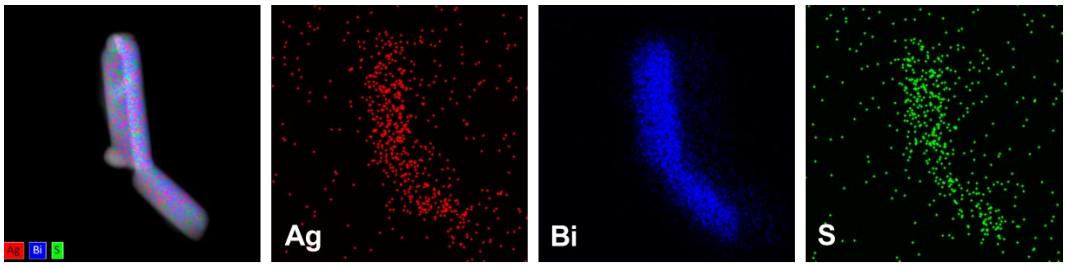

Fig. S31 Elemental mapping images of Ag/Bi_2S_3-10.24%.

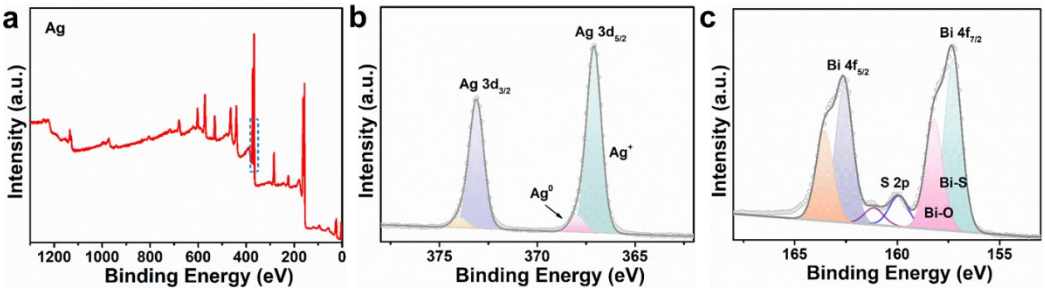

Fig. S32 (a) XPS full spectrum, (b) Ag 3d XPS spectra and (c) Bi 4f XPS spectra of Ag/Bi_2S_3-10.24%.

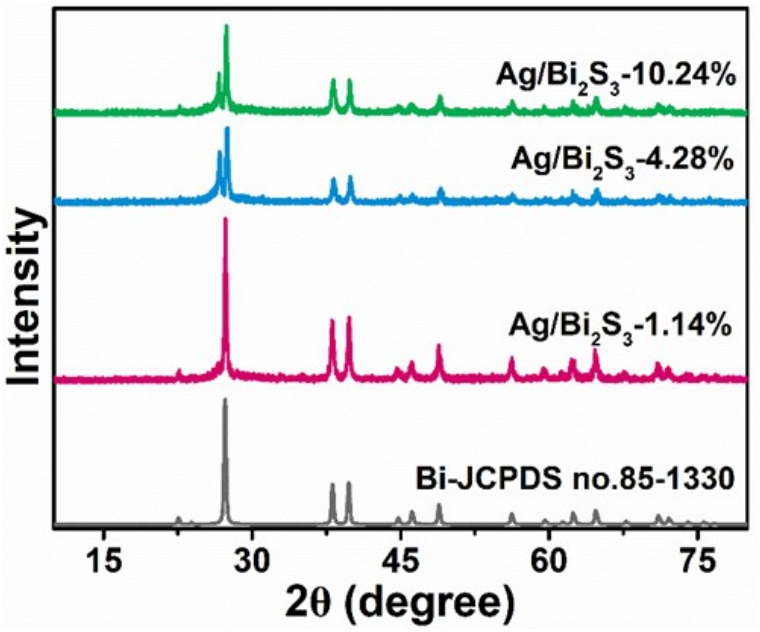

Fig. S33 XRD patterns of Ag/Bi_2S_3-1.14%, Ag/Bi_2S_3-4.28%, and Ag/Bi_2S_3-10.24% after N_2 pretreatment.

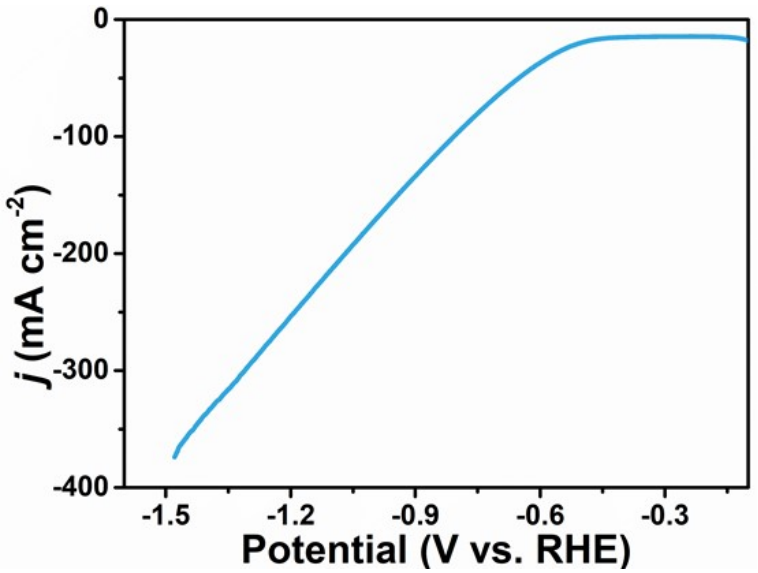

Fig. S34 LSV curves of Cu/Bi_2S_3-2.67% at 1 M KOH electrolyte in flow cell.